

---

# Ising on the Graph: Task-specific Graph Subsampling via the Ising Model

---

**Maria Båkestad**  
Uppsala University  
RISE, Research Institutes of Sweden  
maria.bankestad@ri.se

**Jennifer R. Andersson**  
Uppsala University

**Sebastian Mair**  
Uppsala University

**Jens Sjölund**  
Uppsala University

## Abstract

Reducing a graph while preserving its overall structure is an important problem with many applications. Typically, reduction approaches either remove edges (sparsification) or merge nodes (coarsening) in an unsupervised way with no specific downstream task in mind. In this paper, we present an approach for subsampling graph structures using an Ising model defined on either the nodes or edges and learning the external magnetic field of the Ising model using a graph neural network. Our approach is task-specific as it can learn how to reduce a graph for a specific downstream task in an end-to-end fashion. For this, the task’s loss function does not have to be differentiable. We showcase the versatility of our approach on four distinct applications: image segmentation, explainability for graph classification, 3D shape sparsification, and sparse approximate matrix inverse determination.

## 1 Introduction

Hierarchical organization is a recurring theme in nature and human endeavors [1]. Part of its appeal lies in its interpretability and computational efficiency, especially on uniformly discretized domains such as images or time series [2–5]. On graph-structured data, it is, however, no longer as clear what it means to, e.g., “*sample every second point*”. Solid theoretical arguments favor a spectral approach [6], wherein a simplified graph is found by maximizing the spectral similarity to the original graph [7]. On the other hand, instead of retaining as much of the original information as possible, it may often be more valuable to distill the critical information for the task at hand [8, 9]. The two main approaches for graph simplification, coarsening and sparsification, involve removing nodes and edges. However, it is impossible to tailor coarsening or sparsification to a particular task using existing methods.

We take inspiration from the well-known Ising model in physics [10], which emanated as an analytical tool for studying magnetism but has since undergone many extensions [11, 12]. Within the Ising model, each location is associated with a binary state (interpreted as pointing up or down), and the configuration of all states is associated with an energy.

Thus, the Ising model can be seen as an energy-based model with an energy function comprising a pairwise term and a pointwise “bias” term. As illustrated in Figure 1, the sign of the pairwise term determines whether neighboring states attract or repel each other, while the pointwise term (corresponding to the local magnetic field) controls the propensity of a particular alignment.

In this paper, we consider the Ising model defined on a graph’s nodes or edges and augment it with a graph neural network that models the local magnetic field. There are no particular restrictions on the type of graph neural network, which means that it can, e.g., process multidimensional node and edge features. Since a node (or edge) is either included or not, we use techniques for gradient

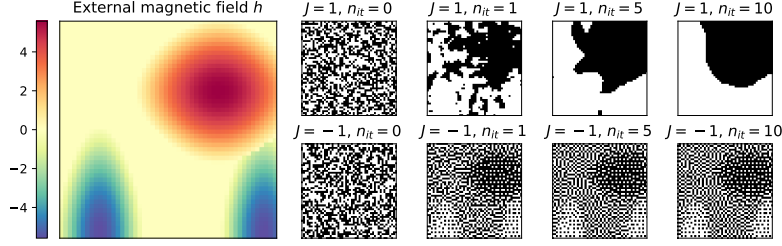


**Figure 1:** The external magnetic field  $h$  (left) can vary spatially and influence the sampling probability relative to its strength. The sign of the coupling constant  $J$  determines whether neighboring spins attract (top right) or repel each other (bottom right).

estimation in discrete models to train our model for a given task. Specifically, we show that the two-point version of the REINFORCE Leave-One-Out estimator (e.g., Shi et al. [13]) results in a straightforward expression and allows for using non-differentiable task-specific losses. To showcase the broad applicability of our model, we demonstrate how it can be used in several domains: image segmentation, explainability for graph classification, 3D shape sparsification, and linear algebra.

## 2 Background

**Energy-based Models.** Energy-based models (EBMs) are defined by an energy function  $E_\theta: \mathbb{R}^d \rightarrow \mathbb{R}$ , parameterized by  $\theta$ . The density defined by an EBM is given by the Boltzmann distribution

$$p_\theta(x) = Z_\theta^{-1} \exp(-\beta E_\theta(x)), \quad (1)$$

where  $\beta > 0$  is the inverse temperature and the normalization constant  $Z = \int \exp(-\beta E_\theta(x)) dx$ , also known as the partition function, is typically intractable.

A sample with low energy will have a higher probability than a sample with high energy. Many approaches have been proposed for training energy-based models [14]. Still, most of them target the generative setting where a training dataset is given and training amounts to (approximate) maximum likelihood estimation.

**Ising Model.** The Ising model corresponds to a deceptively simple energy-based model that is straightforward to express on a graph  $\mathcal{G} = (\mathcal{V}, \mathcal{E})$  consisting of a tuple of a set of nodes  $\mathcal{V}$  and a set of edges  $\mathcal{E} \subseteq \mathcal{V} \times \mathcal{V}$  connecting the nodes. Specifically, the Ising energy is of the form

$$E(x) = - \sum_{(i,j) \in \mathcal{E}} J_{ij} x_i x_j - \sum_{i \in \mathcal{V}} h_i x_i, \quad (2)$$

where the nodes (indices  $i, j$ ) are associated with spins  $x_i \in \{\pm 1\}$ , the interactions  $J_{ij} \in \mathbb{R}$  determine whether the behavior is ferromagnetic ( $J > 0$ ) or antiferromagnetic ( $J < 0$ ), and  $h_i$  is the external magnetic field.

It follows from Equation (2) that in the absence of an external magnetic field, neighboring spins strive to be parallel in the ferromagnetic case and antiparallel in the antiferromagnetic case. An external magnetic field that can vary across nodes influences the sampling probability of the corresponding nodes. The system is disordered at high temperatures (small  $\beta$ ) and ordered at low temperatures.

**Graph Neural Network.** A graph neural network (GNN) consists of multiple message-passing layers [15]. Given a node feature  $x_i^k$  at node  $i$  and edge features  $e_{ij}^k$  between node  $i$  and its neighbors  $\{j: j \in \mathcal{N}(i)\}$ , the message passing procedure at layer  $k$  is defined as

$$m_{ij}^k = f^m(x_i^k, x_j^k, e_{ij}^k), \quad \hat{x}_i^{k+1} = f_j^a(m_{ij}^k), \quad x_i^{k+1} = f^u(x_i^k, \hat{x}_i^{k+1}), \quad (3)$$

where  $f^m$  is the message function, deriving the message from node  $j$  to node  $i$ , and  $f_{j \in \mathcal{N}(i)}^a$  is a function that aggregates the messages from the neighbors of node  $i$ , denoted  $\mathcal{N}(i)$ . The aggregation function  $f^a$  is often just a simple sum or average. Finally,  $f^u$  is the update function that updates the features for each node. A GNN consists of message-passing layers stacked onto each other, where the node output from one layer is the input of the next layer.

Note that we can rewrite the energy in Equation (2) to reveal the message-passing structure of the Ising model as

$$E(x) = - \sum_{i \in \mathcal{V}} x_i \cdot \left( h_i + \sum_{j \in \mathcal{N}(i)} J_{ij} x_j \right) = - \sum_{i \in \mathcal{V}} x_i h_i^{\text{eff}}(x), \quad (4)$$

where we have defined the effective magnetic field

$$h_i^{\text{eff}}(x) = h_i + \sum_{j \in \mathcal{N}(i)} J_{ij} x_j. \quad (5)$$

Equation (4) can be viewed as a message-passing step in a graph neural network, where  $m_{ij}^k = J_{ij} x_j^k$  is the message function  $f^m$ , the aggregation  $f^a$  function is the sum  $\hat{x}_i^{k+1} = \sum_{j \in \mathcal{N}(i)} m_{ij}^k$ , and the update function  $f^u$  is  $x_i^{k+1} = -x_i^k (h_i + \hat{x}_i^{k+1})$ .

**Gradient Estimation in Discrete Models.** Let  $p_\theta(x)$  be a discrete probability distribution and assume that we want to estimate the gradient of a loss defined as the expectation of a loss  $\ell(x)$  over this distribution, i.e.,

$$\mathcal{L}(\theta) = \mathbb{E}_{x \sim p_\theta(x)} [\ell(x)]. \quad (6)$$

Because of the discreteness, it is not possible to compute a gradient directly using backpropagation. Through a simple algebraic manipulation, we can rewrite this expression as

$$\nabla_\theta \mathbb{E}_{x \sim p_\theta(x)} [\ell(x)] = \mathbb{E}_{x \sim p_\theta(x)} [\ell(x) \nabla_\theta \log p_\theta(x)], \quad (7)$$

which is called the REINFORCE estimator [16]. Though general, it suffers from high variance. A way to reduce this variance is to instead use the REINFORCE Leave-One-Out (RLOO) estimator (e.g., Shi et al. [13]),

$$(\nabla_\theta \mathcal{L})_{\text{LOO}}^K = \frac{1}{K} \sum_{k=1}^K \left( \ell(x^{(k)}) - \bar{\ell}_j \right) \nabla_\theta \log p_\theta(x^{(k)}), \quad \text{where } \bar{\ell}_j = \frac{1}{K-1} \sum_{j=1, j \neq k}^K \ell(x^{(j)}). \quad (8)$$

### 3 Method

In graph neural network terminology, the interactions  $J_{ij}$  and the external magnetic fields  $h_i$  could be considered edge and node features, respectively. In particular, we use a GNN to parameterize the external magnetic field,  $h_\theta: \mathcal{G} \rightarrow \mathbb{R}^{|\mathcal{V}|}$ .

**Sampling.** We use the Metropolis-Hastings algorithm to sample from the probability distribution defined by the Ising model according to Equation (1), see Algorithm 1. However, to make it computationally efficient, we parallelize it by first coloring the graph so that nodes of the same color are never neighbors.

Then, we can simultaneously perform the Metropolis-Hastings update for all nodes of the same color. A simple checkerboard pattern perfectly colors grid-structured graphs, such as images. To extend this to general graphs, we run a greedy graph coloring heuristic [17] that produces a coloring with a limited, but not necessarily minimal, number of colors  $C$  (see Appendix B).

**Controlling the Sampling Fraction.** For some tasks, the obvious way to minimize the loss is to either sample all nodes or none. To counteract this, we need a way to control the fraction of nodes to sample or, equivalently, to control the average magnetization  $\eta$ , which is defined as

$$\eta = \frac{1}{|\mathcal{V}|} \sum_{i=1}^{|\mathcal{V}|} \mathbb{E}_{x \sim p_\theta(x)} [x_i], \quad (9)$$

where  $x \in \{\pm 1\}^{|\mathcal{V}|}$  denotes the vector containing all states and  $x_i$  is the  $i$ th entry in  $x$ . Let  $\bar{x}_i = \mathbb{E}_{x \sim p_\theta(x)} [x_i]$  denote the local magnetization at node  $i$ . Since the Markov blanket of a node is precisely its neighborhood, we can use Equation (4) to rewrite the local magnetization as

$$\bar{x}_i = \mathbb{E}_{j \in \mathcal{N}(i)} [\mathbb{E}_i [x_i | x_j]] = \mathbb{E}_{j \in \mathcal{N}(i)} [\tanh(\beta h_i^{\text{eff}}(x))]. \quad (10)$$

---

**Algorithm 1** Monte Carlo Sampling of the Ising Model
 

---

**Input:** Graph  $\{\mathbf{G}_c\}_{c=1}^C$  grouped by color  $c$ , interactions term  $J$ , external magnetic field  $h$ , number of iterations  $T$ .  
**Output:** State configuration  $x \in \{\pm 1\}^{|\mathcal{V}|}$ .  
**for**  $i = 1$  **to**  $|\mathcal{V}|$  **do**  
      $x_i \sim U(\{-1, 1\})$  {Sample an initial state}  
**for**  $t = 1$  **to**  $T$  **do**  
     **for**  $c = 1$  **to**  $C$  **do**  
         **for all nodes**  $x_i \in \mathbf{G}_c$  **do**  
              $\Delta E_i = 2x_i \left( J \sum_{j \in \mathcal{N}(i)} x_j + h_i \right)$   
              $r \sim U([0, 1])$  {Sample  $r$  uniformly at random}  
             **if**  $\Delta E_i < 0$  **or**  $\exp(-2\beta\Delta E_i) > r$  **then**  
                  $x_i = -1 \cdot x_i$  {Flip the spin of node  $i$ }

---

The corresponding mean-field (variational) approximation is a nonlinear system of equations in  $\bar{x}$  [18]:

$$\bar{h}_i^{\text{eff}}(\bar{x}) = h_i + \sum_{j \in \mathcal{N}(i)} J_{ij} \bar{x}_j, \quad \bar{x}_i = \tanh(\beta \bar{h}_i^{\text{eff}}). \quad (11)$$

Solving this yields a deterministic way of approximating the average magnetization  $\eta$ . However, we are primarily interested in the ordered regime, where  $\beta \bar{h}_i^{\text{eff}}$  is large, and it approximately holds that  $x_j = J_{ij} x_i$ , which implies that  $\bar{x}_i = \tanh(\beta h_i)$  and, thus,

$$\tilde{\eta}_{\text{det}} = \frac{1}{|\mathcal{V}|} \sum_{i=1}^{|\mathcal{V}|} \tanh(\beta h_i). \quad (12)$$

This can be contrasted with the stochastic estimate we get from using a one-sample Monte Carlo estimate in Equation (10):

$$\tilde{\eta}_{\text{sto}} = \frac{1}{|\mathcal{V}|} \sum_{i=1}^{|\mathcal{V}|} \tanh(\beta h_i^{\text{eff}}(x)), \quad x \sim p_\theta(x). \quad (13)$$

**Learning.** In contrast to most other energy-based models [14], we do not have a training dataset we want to sample from, nor do we consider the regression setting [19]. Instead, we consider the unsupervised setting where the subsampled graph is used for a downstream task with an associated, possibly non-differentiable, loss.

We need the gradient of the log probability for gradient-based training of the GNN in our Ising model, which can be decomposed as a sum of two terms:

$$\nabla_\theta \log p_\theta(x) = -\beta \nabla_\theta E_\theta(x) - \nabla_\theta \log Z_\theta. \quad (14)$$

We are particularly interested in training the model for a downstream task associated with a loss  $\ell(x)$  defined in terms of samples  $x \sim p_\theta(x)$  from the Ising model. The goal is then to minimize the expected loss as defined in Equation (6).

Since we are operating in a discrete setting, we use the gradient estimation technique described in Section 2. Specifically, using  $K = 2$  in Equation (8), the problematic  $\log Z_\theta$  terms cancel in the RLOO estimator, and we obtain

$$(\nabla_\theta \mathcal{L})_{\text{LOO}}^2 = -\frac{\beta}{2} \left( \ell(x^{(1)}) - \ell(x^{(2)}) \right) \cdot \nabla_\theta \left( E_\theta(x^{(1)}) - E_\theta(x^{(2)}) \right). \quad (15)$$

To train the model, we can thus draw two independent samples  $x^{(1)}, x^{(2)} \sim p_\theta(x)$  from the Ising model and estimate the gradient using Equation (15), where  $\nabla_\theta (E_\theta(x^{(1)}) - E_\theta(x^{(2)}))$  can be computed by automatic differentiation.

To control the sampling fraction, as described in Section 3, we could either include a regularization term that depends on the stochastic sampling fraction (Equation (13)) directly in the task-specific loss  $\ell$ , or use a deterministic approximation based on Equation (12) to move it outside the expectation and thereby enable direct automatic differentiation. Empirically, we found the latter option to work better. Specifically, we use the training loss

$$\mathcal{L}_{\text{tot}}(\theta) = \mathbb{E}_{x \sim p_\theta(x)} [\ell(x)] + (\tilde{\eta}_{\text{det}}(\theta) - \eta)^2, \quad (16)$$

where the desired value of the average magnetization  $\eta$  is defined as in Equation (9).



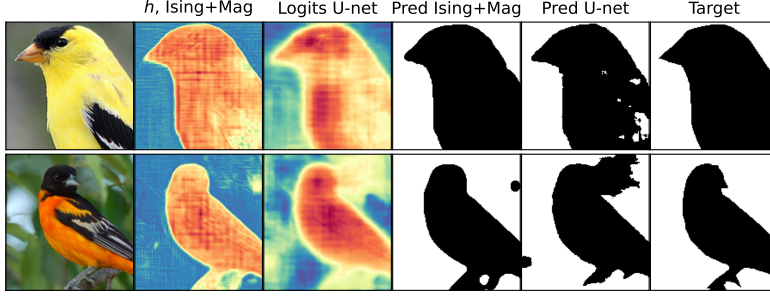


**Figure 2:** Comparison of a U-Net trained with a cross-entropy loss against an Ising model with a learned magnetic field. The sequence from left to right includes the original image, the magnetic field from the Ising model, the U-Net output (the logits), the Ising model prediction, the U-Net prediction, and the actual segmentation mask.

## 4 Applications

The proposed energy-based graph subsampling method is applied across four distinct areas: image segmentation, explainability for graph classification, 3D shape sparsification, and the determination of sparse approximate matrix inverses.

### 4.1 Illustrative Example on Image Segmentation

While the primary goal is to learn Ising models on graphs, we initially delve into an image task due to its visual and explanatory simplicity. An image can fundamentally be seen as a simple graph, with the pixels as nodes and the neighboring pixels as neighbors [20]. Specifically, in the ferromagnetic scenario with  $J = 1$ , Ising models tend to group nearby pixels with the same values. Postprocessing the output of a neural network with such a probabilistic graphical model is well-known to improve the localization of object boundaries [21].

**Our Approach.** Because of the grid structure, the message from the 8-connected neighbors can be implemented as a convolutional layer with kernel size three and zero padding. Specifically, we use convolutional filters of the form

$$W = \begin{bmatrix} w^* & w & w^* \\ w & 0 & w \\ w^* & w & w^* \end{bmatrix}, \quad (17)$$

where  $w$  and  $w^*$  have the same sign but can have different values. This gives us the energy per pixel,

$$E_i = -x_i (\text{Conv}_W(x_i) + h_\theta(x_i)). \quad (18)$$

Here,  $\text{Conv}_W$  is an image convolutional operator with weights  $W$  and  $h_\theta(x_i)$  is the external magnetic field with the learnable parameters  $\theta$ . In contrast to Zheng et al. [22], who use the mean-field approximation in Equation (11) to learn a fully-connected conditional random field end-to-end, our approach applies to graph-structured energy functions and allows task-specific losses.

Since we consider binary segmentation, we use a pixel-wise misclassification loss

$$\ell(x) = \frac{1}{|\mathcal{V}|} \sum_{i=1}^{|\mathcal{V}|} |x_i - y_i|, \quad \text{where the target value is } y_i \in \{-1, 1\}. \quad (19)$$

**Results.** We use the Caltech-UCSD Birds-200-2011 dataset [23] and model the magnetic field of the Ising model by a U-Net [24]. See Appendix C for details.

Directly training the model for segmentation using a standard cross-entropy loss yields an average Dice score of 0.85 on the test set. In contrast, using a learned magnetic field in the Ising model, the average Dice score increases to 0.87 on the test set. Figure 2 compares two predictions from the two models. Notably, the output from the magnetization network of the Ising model exhibits clearer and sharper borders compared to the logits predicted by the plain segmentation model. This distinction is also evident in the predictions, where the segmentation mask predicted by the Ising model is more even and self-consistent.

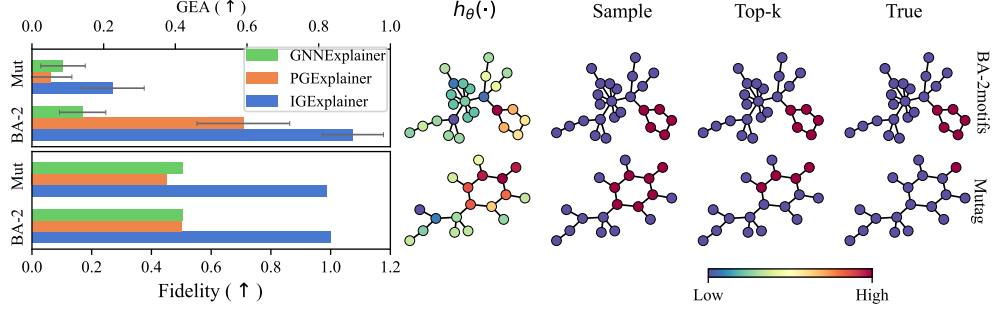


**Figure 3: Left:** Quantitative evaluation of the IGExplainer using a synthetic dataset BA-2motifs and a real-world dataset Mutag. We compare against PGExplainer [26] and GNNExplainer [27]. We report the graph explanation accuracy (GEA) and the fidelity score; higher is better for both scores. The theoretical limit of GEA for Mutag is 0.43. For BA-2motifs, it is 1. **Right:** Qualitative analysis of the explanations generated by the IGExplainer with the magnetic field  $h$ , the sample average, and the top- $k$  nodes.

## 4.2 Explainability for Graph Classification

Graph neural networks integrate information from features with the graph topology. While being a key ingredient of their success, this makes their predictions challenging to explain [25]. Nevertheless, there is a clear need for such explanations in high-stakes applications like drug design. We focus on the most studied class of problems in GNN explainability: graph classification. However, our approach is equally applicable to explain node and edge classifications.

**Our Approach.** Similar to PGExplainer [26], we extract subgraph explanations from a trained (probabilistic) classifier and the corresponding training data. More specifically, we consider a subgraph to be an explanation of whether the model’s prediction on that subgraph agrees with the prediction on the whole graph. In the taxonomy of Kakkad et al. [25], this makes it a perturbation-based post-hoc method. To find such subgraph explanations, we train the external magnetic field of a ferromagnetic Ising model ( $J > 0$ ) by minimizing the cross-entropy between predictions  $y \sim p(y | \mathcal{G})$  for the whole graph  $\mathcal{G}$  and predictions  $y_s \sim p(y | \mathcal{G}_s)$  for sampled subgraphs  $\mathcal{G}_s$ . Specifically, subgraphs are sampled by subsampling nodes according to the Ising model, including all edges between those nodes. In the special case of binary classification, the cross-entropy reduces to the familiar expression

$$H(y, y_s) = -(p \log p_s + (1 - p) \log(1 - p_s)), \quad (20)$$

where we use the shorthand notation  $p := p(y = 1 | \mathcal{G})$  and  $p_s := p(y = 1 | \mathcal{G}_s)$ . To avoid the trivial solution  $\mathcal{G}_s = \mathcal{G}$ , we normalize the external magnetic field to be zero-sum. We call this model the Ising Graph Explainer (IGExplainer).

**Results.** We train our IGExplainer with a three-layer graph isomorphism network (GIN) [28] for modeling the magnetic field  $h_\theta(\cdot)$  and the cross-entropy in Equation (20) as our task-specific loss. We evaluate the method on two standard explainability datasets: BA-2Motifs [26] and Mutag [29, 30]. First, we train a classification model  $\mathcal{M}$  on the dataset (also a GIN network). We then use  $\mathcal{M}$  to derive the loss for the IGExplainer using  $p$  and  $p_s$ . We evaluate predicted explanations using the graph explanation accuracy (GEA) [30]; we select the top- $k$  of the nodes, using  $h_\theta(\cdot)$  as the score. For BA-2motifs, we use  $k = 5$  and for Mutag,  $k$  is 25% of the number of the graph.

We also evaluate the methods’ fidelity [31], which measures how well  $y_s$  matches  $y$ . Here, we use a single sample of the IGExplainer to get the important nodes (on average 34% of the nodes). For the baselines, we select the top 40% of the nodes, not to favor IGExplainer. Figure 3 (left) shows that our IGExplainer outperforms both baselines (PGExplainer [26] and GNNExplainer [27]) in GEA and fidelity. Figure 3 (right) visualizes  $h_\theta(\cdot)$  for one graph from each dataset, where the magnetic field’s strength indicates the node’s importance. We also visualize the sample average, which shows the IGExplainers’ preference for sampling groups of nodes close to each other, contributing to the high fidelity of the IGExplainer. See Appendix D for details on the model, experiments, and datasets.

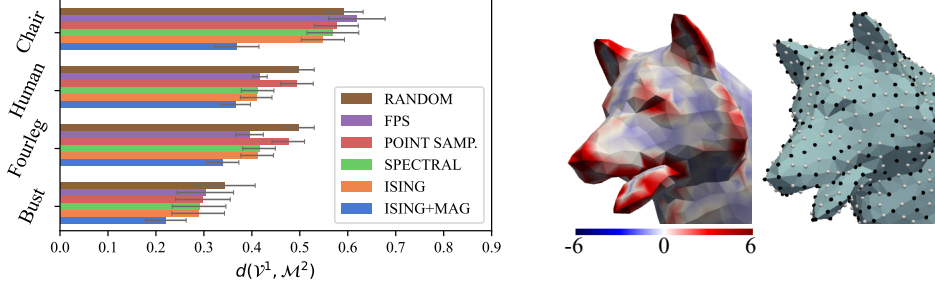


**Figure 4:** **Left:** Mean and standard deviation of the test vertex-to-mesh distance from the five-fold cross-validation of the four datasets. Here, lower is better. For an explanation of the other methods and the results as a table, see Appendix E. **Middle:** Learned magnetic field of an object. **Right:** Sampled vertices using the Ising model with a learned magnetic field. Black vertices are retained in the coarser mesh and are more important for the overall shape preservation (see the ears and nose).

### 4.3 3D Shape Sparsification

An object’s 3D mesh tends to have a densely sampled surface, resulting in numerous redundant vertices. These redundant vertices increase the computational workload in subsequent processing stages. Consequently, mesh sparsification (representing the object with fewer vertices and edges) is a common preprocessing step, e.g., in computer graphics [32]. The main techniques for sparsifying a mesh are based on preserving the spectral properties of the original mesh [33, 34]. However, these methods cannot be adapted to specific downstream tasks.

A triangular mesh  $\mathcal{M}$  is composed of vertices  $\mathcal{V}$ , edges  $\mathcal{E}$ , and faces  $\mathcal{F}$ , where the faces define the triangles formed by the vertices. To sparsify the mesh, we remove selected vertices and collapse the connected edges to their nearest neighboring vertex. To simplify the process, we keep the vertices’ positions fixed, avoiding the added complexity of repositioning them, which would make it harder to assess the impact of the sampling. The distance between the vertices  $\mathcal{V}^1$  of the original mesh and the surface of the coarser mesh  $\mathcal{M}^2$  is defined as:

$$d(\mathcal{V}^1, \mathcal{M}^2) = \sum_{x \in \mathcal{V}^1} \min_{y \in \mathcal{M}^2} \|x - y\|_2^2. \quad (21)$$

For each vertex in mesh  $\mathcal{M}^1$ , the algorithm finds the nearest point on mesh  $\mathcal{M}^2$  and sums the squared distances.

**Our approach.** We approach mesh sparsification as a sampling problem, using the antiferromagnetic Ising model to select vertices for the coarse mesh. This model is well-suited because its “every other” pattern helps to distribute the samples more evenly across the mesh. Additionally, the magnetic field  $h_\theta(x)$  guides sampling toward regions that are most relevant to the task, i.e., shape preservation.

The 3D shapes are presented as graphs, using vertex positions as node features and relative distances between nodes as edge features,  $e_{ij} = x_i - x_j$ . To model the magnetic field  $h_\theta(\cdot)$ , we use a three-layer Euclidean graph neural network [35], which captures 3D geometric information while being equivariant to rotations and translations. We also use the mesh Laplacian [36] to measure surface geometry (see Appendix E).

**Results.** We use the vertex-to-mesh distance in Equation (21) as our task-specific loss and train the Ising model on four different mesh datasets [37]: *bust*, *four-leg*, *human*, and *chair*, where each dataset contains 20 different meshes. We evaluate the model using five-fold cross-validation. We train the models until convergence on the training dataset, using  $\eta = 0$  in Equation (16), aiming to reduce the number of vertices in each mesh by half.

Figure 4 demonstrates that the Ising model with the magnetic field (ISING+MAG) achieves the lowest point-to-mesh distance since it is trained for this specific task. ISING and Spectral coarsening (SPECTRAL) [6] perform similarly, both producing an every-other pattern, where SPECTRAL selects nodes via the graph Laplacian’s largest eigenvector. While furthest point sampling (FPS) [38] distributes points evenly, it misses key areas. ISING+MAG combines geometric insights with

effective mesh preservation. Additional details on the model, dataset, baselines, and time complexity are presented in Appendix E.

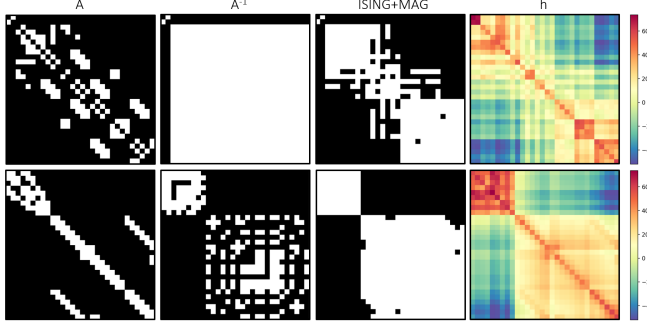


**Table 1:** Mean and standard deviation of the loss in Equation (23) over the test set for each setting and model using a single sample from the learned Ising model. Lower is better.

Model	Setting 1	Setting 2	Setting 3
ISING+MAG	<b>3.28</b> (0.12)	<b>2.06</b> (0.26)	<b>1.15</b> (1.24)
ISING	3.86 (0.12)	3.69 (0.23)	3.78 (0.42)
RANDOM	4.04 (0.16)	3.86 (0.18)	3.86 (0.30)
ONLY A	4.12 (0.08)	4.12 (0.08)	2.00 (1.89)

**Figure 5:** Two test matrices. The sparsity of  $A$  (non-zeros are white), sparsity of  $A^{-1}$ , sparsity of our sparse approximate inverse using 50% of all matrix elements (*Setting 3*), and the predicted magnetic field  $h$ .

#### 4.4 Sparse Approximate Matrix Inverses

Large linear systems  $Az = b$ , where  $A \in \mathbb{R}^{n \times n}$  is a sparse matrix, are frequently solved in many scientific and technical domains. With increasing problem size, direct methods are replaced by iterative methods, e.g., Krylov subspace methods. However, if the problem is ill-conditioned, these methods require preconditioning [39] for which sparse approximate inverses (SAIs) are often suitable.

More precisely, we aim to find a sparse approximate inverse  $M \approx A^{-1} \in \mathbb{R}^{n \times n}$  representing a right preconditioner for the sparse linear system  $Az = b$ . Let  $I$  be the identity matrix,  $s \in \mathcal{S}$  be the sparsity pattern of the matrix  $M$ , where  $\mathcal{S}$  is the space of all sparsity patterns,  $s$  contains the  $m$  indices of the non-zero matrix entries, and  $s' \in \mathbb{R}^m$  contains the non-zero values. Further, let  $M'(s)$  denote the approximate inverse with sparsity pattern  $s$  and non-zeros  $s'$  which we find by solving

$$\min_{s' \in \mathbb{R}^m} \|AM'(s) - I\|_F. \quad (22)$$

The problem is that this approach requires an a priori assumption on  $s$  which affects the quality of the preconditioner. Various modifications to the described sparse approximate inverse approach exist, aiming to refine the sparsity pattern iteratively [40].

**Our Approach.** Symmetric sparse linear systems can be represented as graphs [41] where  $A$  is viewed as the adjacency matrix of a weighted undirected graph where the matrix elements correspond to edge features. The idea is to use the Ising model to sample sparsity patterns of the SAI. However, our Ising model is defined over nodes; hence, we move the graph representation to its line graph [42]. A sample  $x$  from our model corresponds to a proposed sparsity pattern  $s$  of the predicted SAI  $M$ . As before, we parametrize our model by  $\theta$  and learn it by minimizing Equation (16) using  $\eta = 0$  and

$$l(x) = \|AM(s_\theta(x)) - I\|_F. \quad (23)$$

Here, we aim to reduce the number of elements of an a priori sparsity pattern (possibly including all elements) by 50%. We obtain the specific SAI  $M(s_\theta(x))$  by solving Equation (22) using the sampled sparsity pattern of the Ising model given its current parameters. The external magnetic field is modeled by a graph GCN [43], and we use the RLOO gradient estimator according to Equation (15). Besides,  $A$  and  $A^2$  enter as edge features. Contrary to conventional approaches, our method is flexible in terms of a priori sparsity patterns. Appendices F.1 and F.2 contain further details.

**Datasets.** *Dataset 1* consists of 1600 synthetic binary sparse matrices of size  $30 \times 30$  and *Dataset 2* consists of 1800 sparse  $30 \times 30$  submatrices constructed from the SuiteSparse Matrix Collection [44], thus resembling real-world sparse matrices. We use 60%, 20%, and 20% for training, validation, and testing, respectively. Further details on the datasets and preprocessing can be found in Appendix F.3.

**Results.** We consider three settings. *Setting 1* uses  $A$  and  $A^2$  as edge features on *Dataset 1*. Here, the a priori sparsity pattern of the SAI is the same as for  $A^2$  and our model selects 50% of those positions for  $M$ . *Setting 2* is similar but allows for using 50% of all positions. *Setting 3* is as *Setting 2* but on *Dataset 2*. Appendix F.1 contains implementation details.

Figure 5 depicts two test samples from *Setting 3* on how the learned magnetic field has adapted to allow for sampling of a suitable sparsity pattern when the true inverses have inherently different structures. The results are detailed in Appendix F.1. Table 1 shows the performance of our model (ISING+MAG) compared to three baselines: (i) an Ising model with a small constant magnetic field tuned to obtain the same sampling fraction as on the corresponding test set (ISING), (ii) uniform random sampling from the allowed sparsity pattern in each setting with the corresponding sampling fraction (RANDOM), and (iii) the quality of the sparse approximate inverse obtained using only the sparsity pattern of the input  $A$  (ONLY A). In all cases, ISING+MAG yields significant improvements.

## 5 Related Work

**Statistical Physics.** The Ising model was one of the first tractable analytical models of magnetic systems that exhibit phase transitions. Interestingly, the closer the parameter is to its critical value, the less the details of the system matter. This observation, referred to as universality in statistical physics, has motivated the generalization of the Ising model to broader classes of systems. For instance, the standard Potts model is a generalization of the Ising model to multiple classes [11]. By contrast, the Ising model with random interactions  $J_{ij}$  is a form of spin glass system [12] closely related to Hopfield networks [18]: A model of associative memory that has recently experienced a resurgence [45–47].

**Probabilistic Graphical Models.** The Ising model, or spin glasses more generally, gave rise to the concept of a Markov random field, where a probabilistic graphical model [48] is used to encode dependencies between random variables. In our model, we output the external magnetic field as an intermediate variable that we then condition on to define an Ising model. It is, therefore, appropriately described as a conditional random field [49]. Conditional random fields are widely used for structured prediction tasks, for instance, in natural language processing [50] and computer vision [21, 22].

**Graph Sparsification and Coarsening.** The goal of graph sparsification and coarsening operations is to generate a smaller graph that preserves the global structure of a large graph. A unifying framework that captures both of these operations is considered by Bravo-Hermesdorff and Gunderson [51]. In contrast to our approach, theirs is not learned; rather, they present an algorithm for reducing a graph while preserving the Laplacian pseudoinverse. Many algorithms for graph coarsening aim to preserve spectral properties [7, 52–54]. Building on top of this idea are approaches based on neural networks [8]. A graph coarsening can also be computed based on optimal transport [55], graph fusion [56], and Schur complements with the goal of obtaining embeddings of relevant nodes [57]. The coarsening of graphs is also done for the scalability of GNNs [58] and dataset condensation [9, 59]. The goal is that GNNs perform similarly on the condensed data but are faster to train. Finally, Chen et al. [33] provides an overview of successful coarsening techniques for scientific computing. As for graph sparsification, spectral sparsification [60] and information-theoretic formulations [61] can be used. Graph partitioning can be done using quantum annealing by minimizing an Ising objective [62]. Batson et al. [63] provides an overview on the topic of sparsification, and Hashemi et al. [64] presents a general survey on graph reduction, including sparsification, coarsening, and condensation.

## 6 Discussion and Conclusion

We proposed a new method for graph subsampling by first learning the external magnetic field in the Ising model and then sampling from the resulting distribution. Our approach has shown potential in various applications and does not require the differentiability of the loss function of a given application. We achieved this using the REINFORCE Leave-One-Out gradient estimator and a carefully chosen regularization structure that allowed us to adjust the sampling fraction. Within a diverse set of experiments on four applications, we demonstrated the effectiveness of our method. In image segmentation, our approach generated segmentation masks with sharp borders. Our IGExplainer produced explanations with high accuracy and fidelity for graph classification. In mesh coarsening, the learned magnetic field increased the sampling rate in high-curvature regions while maintaining the characteristic “every other” pattern. Finally, we illustrated that our approach can learn sparsity patterns for determining sparse approximate matrix inverses via Frobenius norm minimization.

**Limitations and Future Work.** For our applications, the computations were fast (see Figures 17 and 18 in Appendix E), but this may change for other large-scale applications, where the sampling (incl. graph coloring) can become a bottleneck. This is something we want to address in future work. Another limitation is that the Ising model only allows for binary states, whereas some applications,



e.g., image classification, require multiple classes. We believe it is possible to extend our approach to such cases by instead using the Potts model or the even more general random cluster model [65].

**Acknowledgments** This work was partially supported by the Wallenberg AI, Autonomous Systems and Software Program (WASP) funded by the Knut and Alice Wallenberg Foundation.

## References

- [1] Denise Pumain, editor. *Hierarchy in Natural and Social Sciences*, volume 3 of *Methodos Series*. Springer Dordrecht, 2006. 1
- [2] Pierre Duhamel and Martin Vetterli. Fast Fourier transforms: a tutorial review and a state of the art. *Signal Processing*, 19(4):259–299, 1990. 1
- [3] Stéphane Mallat. *A wavelet tour of signal processing*. Elsevier, 1999.
- [4] Wolfgang Hackbusch. *Multi-grid methods and applications*, volume 4. Springer Science & Business Media, 2013.
- [5] Tony Lindeberg. *Scale-space theory in computer vision*, volume 256. Springer Science & Business Media, 2013. 1
- [6] David I Shuman, Mohammad Javad Faraji, and Pierre Vandergheynst. A multiscale pyramid transform for graph signals. *IEEE Transactions on Signal Processing*, 64(8):2119–2134, 2015. 1, 7, 20
- [7] Yu Jin, Andreas Loukas, and Joseph JaJa. Graph coarsening with preserved spectral properties. In *International Conference on Artificial Intelligence and Statistics*, pages 4452–4462. PMLR, 2020. 1, 9
- [8] Chen Cai, Dingkan Wang, and Yusu Wang. Graph coarsening with neural networks. In *International Conference on Learning Representations*, 2021. 1, 9
- [9] Wei Jin, Xianfeng Tang, Haoming Jiang, Zheng Li, Danqing Zhang, Jiliang Tang, and Bing Yin. Condensing graphs via one-step gradient matching. In *Proceedings of the 28th ACM SIGKDD Conference on Knowledge Discovery and Data Mining*, pages 720–730, 2022. 1, 9
- [10] Barry A Cipra. An introduction to the Ising model. *The American Mathematical Monthly*, 94(10):937–959, 1987. 1
- [11] Fa-Yueh Wu. The Potts model. *Reviews of Modern Physics*, 54(1):235, 1982. 1, 9
- [12] Hidetoshi Nishimori. *Statistical physics of spin glasses and information processing: an introduction*. Clarendon Press, 2001. 1, 9
- [13] Jiaxin Shi, Yuhao Zhou, Jessica Hwang, Michalis Titsias, and Lester Mackey. Gradient estimation with discrete stein operators. In *Advances in Neural Information Processing Systems*, volume 35, pages 25829–25841, 2022. 2, 3
- [14] Yang Song and Diederik P Kingma. How to train your energy-based models. *arXiv preprint arXiv:2101.03288*, 2021. 2, 4
- [15] Justin Gilmer, Samuel S Schoenholz, Patrick F Riley, Oriol Vinyals, and George E Dahl. Neural message passing for quantum chemistry. In *International Conference on Machine Learning*, pages 1263–1272. PMLR, 2017. 2
- [16] Ronald J Williams. Simple statistical gradient-following algorithms for connectionist reinforcement learning. *Machine Learning*, 8:229–256, 1992. 3
- [17] Gary L Miller, Dafna Talmor, and Shang-Hua Teng. Optimal coarsening of unstructured meshes. *Journal of Algorithms*, 31(1):29–65, 1999. 3
- [18] David JC MacKay. *Information theory, inference and learning algorithms*. Cambridge University Press, 2003. 4, 9
- [19] Fredrik K Gustafsson, Martin Danelljan, Radu Timofte, and Thomas B Schön. How to train your energy-based model for regression. In *Proceedings of the British Machine Vision Conference (BMVC)*, September 2020. 4
- [20] Stuart Geman and Donald Geman. Stochastic relaxation, Gibbs distributions, and the Bayesian restoration of images. *IEEE Transactions on Pattern Analysis and Machine Intelligence*, 6: 721–741, 1984. 5

- [21] Liang-Chieh Chen, George Papandreou, Iasonas Kokkinos, Kevin Murphy, and Alan L Yuille. DeepLab: Semantic image segmentation with deep convolutional nets, atrous convolution, and fully connected CRFs. *IEEE Transactions on Pattern Analysis and Machine Intelligence*, 40(4): 834–848, 2017. 5, 9
- [22] Shuai Zheng, Sadeep Jayasumana, Bernardino Romera-Paredes, Vibhav Vineet, Zhizhong Su, Dalong Du, Chang Huang, and Philip HS Torr. Conditional random fields as recurrent neural networks. In *Proceedings of the IEEE International Conference on Computer Vision*, pages 1529–1537, 2015. 5, 9
- [23] C. Wah, S. Branson, P. Welinder, P. Perona, and S. Belongie. Mesh segmentations. Technical Report CNS-TR-2011-001, California Institute of Technology, 2011. 5
- [24] Olaf Ronneberger, Philipp Fischer, and Thomas Brox. U-net: Convolutional networks for biomedical image segmentation. In *Medical Image Computing and Computer-Assisted Intervention – MICCAI 2015*, pages 234–241. Springer, 2015. 5
- [25] Jaykumar Kakkad, Jaspal Jannu, Kartik Sharma, Charu Aggarwal, and Sourav Medya. A survey on explainability of graph neural networks. *IEEE Data Eng. Bull.*, 46(2):35–63, 2023. 6
- [26] Dongsheng Luo, Wei Cheng, Dongkuan Xu, Wenchao Yu, Bo Zong, Haifeng Chen, and Xiang Zhang. Parameterized explainer for graph neural network. In *Advances in Neural Information Processing Systems*, volume 33, pages 19620–19631, 2020. 6, 16, 17
- [27] Zhitao Ying, Dylan Bourgeois, Jiaxuan You, Marinka Zitnik, and Jure Leskovec. Gnnexplainer: Generating explanations for graph neural networks. In *Advances in Neural Information Processing Systems*, volume 32, 2019. 6, 17
- [28] Keyulu Xu, Weihua Hu, Jure Leskovec, and Stefanie Jegelka. How powerful are graph neural networks? *arXiv preprint arXiv:1810.00826*, 2018. 6, 17
- [29] Jeroen Kazius, Ross McGuire, and Roberta Bursi. Derivation and validation of toxicophores for mutagenicity prediction. *Journal of Medicinal Chemistry*, 48(1):312–320, 2005. 6, 16
- [30] Chirag Agarwal, Owen Queen, Himabindu Lakkaraju, and Marinka Zitnik. Evaluating explainability for graph neural networks. *Scientific Data*, 10(1):144, 2023. 6, 16
- [31] Hao Yuan, Haiyang Yu, Shurui Gui, and Shuiwang Ji. Explainability in graph neural networks: A taxonomic survey. *IEEE Transactions on Pattern Analysis and Machine Intelligence*, 45(5): 5782–5799, 2022. 6
- [32] John Wright, Yi Ma, Julien Mairal, Guillermo Sapiro, Thomas S Huang, and Shuicheng Yan. Sparse representation for computer vision and pattern recognition. *Proceedings of the IEEE*, 98(6):1031–1044, 2010. 7
- [33] Jie Chen, Yousef Saad, and Zechen Zhang. Graph coarsening: from scientific computing to machine learning. *SeMA Journal*, pages 1–37, 2022. 7, 9
- [34] Alexandros Dimitrios Keros and Kartic Subr. Generalized spectral coarsening. *arXiv preprint arXiv:2207.01146*, 2022. 7
- [35] Mario Geiger and Tess Smidt. e3nn: Euclidean neural networks. *arXiv preprint arXiv:2207.09453*, 2022. 7, 19
- [36] Martin Reuter, Silvia Biasotti, Daniela Giorgi, Giuseppe Patanè, and Michela Spagnuolo. Discrete Laplace–Beltrami operators for shape analysis and segmentation. *Computers & Graphics*, 33(3):381–390, 2009. 7
- [37] Xiaobai Chen, Aleksey Golovinskiy, and Thomas Funkhouser. A benchmark for 3d mesh segmentation. *ACM Transactions on Graphics (TOG)*, 28(3):1–12, 2009. 7
- [38] Yuval Eldar, Michael Lindenbaum, Moshe Porat, and Yehoshua Y Zeevi. The farthest point strategy for progressive image sampling. *IEEE Transactions on Image Processing*, 6(9):1305–1315, 1997. 7, 20
- [39] Paul Häusner, Ozan Öktem, and Jens Sjölund. Neural incomplete factorization: learning preconditioners for the conjugate gradient method. *arXiv preprint arXiv:2305.16368*, 2023. 8
- [40] Marcus J Grote and Thomas Huckle. Parallel preconditioning with sparse approximate inverses. *SIAM Journal on Scientific Computing*, 18(3):838–853, 1997. 8
- [41] Nicholas S Moore, Eric C Cyr, Peter Ohm, Christopher M Siefert, and Raymond S Tuminaro. Graph neural networks and applied linear algebra. *arXiv preprint arXiv:2310.14084*, 2023. 8



- [42] Jens Sjölund and Maria Bånkestad. Graph-based neural acceleration for nonnegative matrix factorization. *arXiv preprint arXiv:2202.00264*, 2022. 8
- [43] Ming Chen, Zhewei Wei, Zengfeng Huang, Bolin Ding, and Yaliang Li. Simple and deep graph convolutional networks. In *International Conference on Machine Learning*, pages 1725–1735. PMLR, 2020. 8, 24
- [44] Timothy A. Davis and Yifan Hu. The university of florida sparse matrix collection. *ACM Transactions on Mathematical Software*, 38(1):1–25, 2011. 8, 25
- [45] Dmitry Krotov and John J Hopfield. Dense associative memory for pattern recognition. In *Advances in Neural Information Processing Systems*, volume 29, 2016. 9
- [46] Mete Demircigil, Judith Heusel, Matthias Löwe, Sven Upgang, and Franck Vermet. On a model of associative memory with huge storage capacity. *Journal of Statistical Physics*, 168:288–299, 2017.
- [47] Hubert Ramsauer, Bernhard Schäfl, Johannes Lehner, Philipp Seidl, Michael Widrich, Lukas Gruber, Markus Holzleitner, Thomas Adler, David Kreil, Michael K Kopp, et al. Hopfield networks is all you need. In *International Conference on Learning Representations*, 2020. 9
- [48] Daphne Koller and Nir Friedman. *Probabilistic graphical models: principles and techniques*. MIT Press, 2009. 9
- [49] John D Lafferty, Andrew McCallum, and Fernando CN Pereira. Conditional random fields: Probabilistic models for segmenting and labeling sequence data. In *Proceedings of the International Conference on Machine Learning*, pages 282–289, 2001. 9
- [50] Guillaume Lample, Miguel Ballesteros, Sandeep Subramanian, Kazuya Kawakami, and Chris Dyer. Neural architectures for named entity recognition. In *Proceedings of the 2016 Conference of the North American Chapter of the Association for Computational Linguistics: Human Language Technologies*, pages 260–270, 2016. 9
- [51] Gecia Bravo-Hermesdorff and Lee Gunderson. A unifying framework for spectrum-preserving graph sparsification and coarsening. In *Advances in Neural Information Processing Systems*, volume 32, 2019. 9
- [52] Ilya Safro, Peter Sanders, and Christian Schulz. Advanced coarsening schemes for graph partitioning. *Journal of Experimental Algorithmics*, 19:1–24, 2015. 9
- [53] Andreas Loukas and Pierre Vandergheynst. Spectrally approximating large graphs with smaller graphs. In *International Conference on Machine Learning*, pages 3237–3246. PMLR, 2018.
- [54] Andreas Loukas. Graph reduction with spectral and cut guarantees. *Journal of Machine Learning Research*, 20(116):1–42, 2019. 9
- [55] Tengfei Ma and Jie Chen. Unsupervised learning of graph hierarchical abstractions with differentiable coarsening and optimal transport. In *Proceedings of the AAAI Conference on Artificial Intelligence*, pages 8856–8864, 2021. 9
- [56] Chenhui Deng, Zhiqiang Zhao, Yongyu Wang, Zhiru Zhang, and Zhuo Feng. Graphzoom: A multi-level spectral approach for accurate and scalable graph embedding. In *International Conference on Learning Representations*, 2020. 9
- [57] Matthew Fahrbach, Gramoz Goranci, Richard Peng, Sushant Sachdeva, and Chi Wang. Faster graph embeddings via coarsening. In *International Conference on Machine Learning*, pages 2953–2963. PMLR, 2020. 9
- [58] Zengfeng Huang, Shengzhong Zhang, Chong Xi, Tang Liu, and Min Zhou. Scaling up graph neural networks via graph coarsening. In *Proceedings of the 27th ACM SIGKDD Conference on Knowledge Discovery & Data Mining*, pages 675–684, 2021. 9
- [59] Wei Jin, Lingxiao Zhao, Shichang Zhang, Yozen Liu, Jiliang Tang, and Neil Shah. Graph condensation for graph neural networks. In *International Conference on Learning Representations*, 2022. 9
- [60] Daniel A Spielman and Shang-Hua Teng. Spectral sparsification of graphs. *SIAM Journal on Computing*, 40(4):981–1025, 2011. 9
- [61] Shujian Yu, Francesco Alesiani, Wenzhe Yin, Robert Jenssen, and Jose C Principe. Principle of relevant information for graph sparsification. In *Uncertainty in Artificial Intelligence*, pages 2331–2341. PMLR, 2022. 9

- [62] Hayato Ushijima-Mwesigwa, Christian FA Negre, and Susan M Mniszewski. Graph partitioning using quantum annealing on the d-wave system. In *Proceedings of the Second International Workshop on Post Moores Era Supercomputing*, pages 22–29, 2017. [9](#)
- [63] Joshua Batson, Daniel A Spielman, Nikhil Srivastava, and Shang-Hua Teng. Spectral sparsification of graphs: theory and algorithms. *Communications of the ACM*, 56(8):87–94, 2013. [9](#)
- [64] Mohammad Hashemi, Shengbo Gong, Juntong Ni, Wenqi Fan, B Aditya Prakash, and Wei Jin. A comprehensive survey on graph reduction: Sparsification, coarsening, and condensation. In *Proceedings of the Thirty-Third International Joint Conference on Artificial Intelligence*, 2024. [9](#)
- [65] Cornelius Marius Fortuin and Piet W Kasteleyn. On the random-cluster model: I. introduction and relation to other models. *Physica*, 57(4):536–564, 1972. [10](#)
- [66] Adrian Kosowski and Krzysztof Manuszewski. Classical coloring of graphs. *Contemporary Mathematics*, 352:1–20, 2004. [15](#)
- [67] Aric Hagberg, Pieter J Swart, and Daniel A Schult. Exploring network structure, dynamics, and function using networkx. Technical report, Los Alamos National Laboratory (LANL), Los Alamos, NM (United States), 2008. [15](#)
- [68] Diederik Kingma and Jimmy Ba. Adam: A method for stochastic optimization. In *International Conference on Learning Representations*, 2015. [16](#), [17](#), [19](#), [24](#)
- [69] Matthias Fey and Jan E. Lenssen. Fast graph representation learning with PyTorch Geometric. In *ICLR Workshop on Representation Learning on Graphs and Manifolds*, 2019. [17](#)
- [70] Weihua Hu, Bowen Liu, Joseph Gomes, Marinka Zitnik, Percy Liang, Vijay Pande, and Jure Leskovec. Strategies for pre-training graph neural networks. *arXiv preprint arXiv:1905.12265*, 2019. [17](#)
- [71] Olga Sorkine. Laplacian mesh processing. *Eurographics (State of the Art Reports)*, 4(4), 2005. [19](#)
- [72] Charles Ruizhongtai Qi, Li Yi, Hao Su, and Leonidas J Guibas. Pointnet++: Deep hierarchical feature learning on point sets in a metric space. In *Advances in Neural Information Processing Systems*, volume 30, 2017. [20](#)
- [73] Rolandos Alexandros Potamias, Stylianos Ploumpis, and Stefanos Zafeiriou. Neural mesh simplification. In *Proceedings of the IEEE/CVF Conference on Computer Vision and Pattern Recognition*, pages 18583–18592, 2022. [20](#)

## Appendix

The appendix first presents some details on Ising sampling and graph coloring. It then continues with extra information on our four applications. We only use a single GPU, namely a NVIDIA GeForce RTX 3090, for all applications and performed all experiments using less than 10 GPU hours.

### Contents

<b>A</b>	<b>Ising Sampling</b>	<b>14</b>
<b>B</b>	<b>Graph Coloring</b>	<b>15</b>
<b>C</b>	<b>Binary Segmentation Details</b>	<b>16</b>
<b>D</b>	<b>Explainability for Graph Classification Details</b>	<b>16</b>
D.1	Datasets . . . . .	16
D.2	Baselines . . . . .	17
D.3	Implementation Details . . . . .	17
D.4	Extra Results . . . . .	17
<b>E</b>	<b>Mesh Coarsening</b>	<b>19</b>
E.1	Dataset . . . . .	19
E.2	Implementation Details . . . . .	19
E.3	Baselines . . . . .	20
E.4	Training Time . . . . .	20
E.5	Extra Results . . . . .	20
<b>F</b>	<b>Sparse Approximate Matrix Inverses</b>	<b>24</b>
F.1	Results and Implementation Details . . . . .	24
F.2	Graph Convolutional Neural Network . . . . .	24
F.3	Datasets . . . . .	25

### A Ising Sampling

To illustrate the convergence rate of the Ising model, we plot the energy against the number of Monte Carlo iterations in Figure 6. These simulations are done on the 20 meshes in the Bust dataset of Section 4.3. We plot the mean plus one standard deviation of the model energy at each iteration. We observe that the ferromagnetic ( $J = 1$ ) and antiferromagnetic ( $J = -1$ ) Ising models converge fast, even though the antiferromagnetic one converges faster in just a handful of iterations.

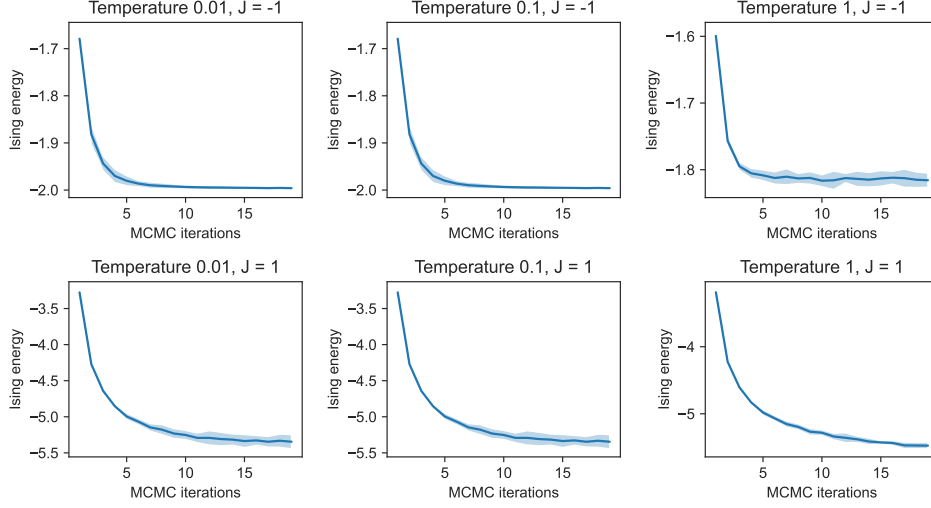


**Figure 6:** The mean and standard deviation of the Ising model energy against the number of Monte Carlo iterations for the ( $J = 1$ ) or antiferromagnetic ( $J = -1$ ) Ising model. The simulation is also done for three different temperatures: 0.01, 0.1, and 1.

## B Graph Coloring

The graph coloring is based on the greedy graph coloring algorithm explained in [66]. We use the implementation of NetworkX [67]. The computational complexity of the greedy coloring method is  $\mathcal{O}(m + n)$ , where  $n$  is the number of vertices and  $m$  is the number of edges in the graph. Figure 7 shows the coloring time plotted against the number of vertices for the graph coarsening dataset of Section 4.3. This indicates that the time taken for coloring is insignificant compared to the time required for sampling and coarsening. However, the coloring time could potentially become problematic for exceptionally large graphs. It's worth noting that coloring an image is extremely fast and straightforward due to its simple structure.

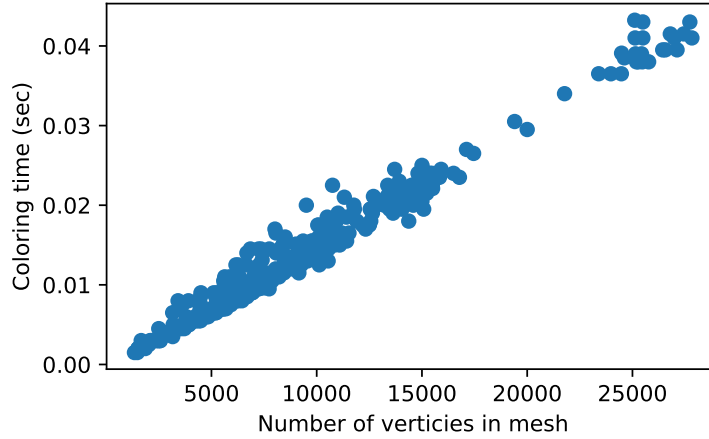


**Figure 7:** The time it takes to color a graph, plotted against the number of vertices in the graph.

## C Binary Segmentation Details

We train a U-Net for the bird segmentation task in Section 4.1 using three down-sampling blocks, one middle layer, and three up-sampling blocks. The implementation is inspired by <https://github.com/yassouali/pytorch-segmentation/tree/master>. The dimensions of the blocks/layers are presented in Table 2.

**Table 2:** Dimensions of the U-Net blocks.

LAYER	INPUT DIM	OUTPUT DIM
INPUT LAYER	3	16
ENCODER 1	16	32
ENCODER 2	32	64
ENCODER 3	64	128
MID LAYER	128	128
DECODER 1	128	64
DECODER 2	64	32
DECODER 3	32	16
OUTPUT LAYER	16	1

We train the model using the Adam optimizer [68], a batch size of 32, and a learning range of  $1e - 4$ . The dataset contains 6537 segmented images. We split the dataset in a train/val/test split using the ratios 0.8/0.1/0.1. We train the model for 300 epochs and test the model with the lowest validation error. Here, the Ising model uses a temperature of one and  $J = 1$ .

## D Explainability for Graph Classification Details

This section contains the details of the explaining graph classification experiments of Section 4.2.

### D.1 Datasets

The *BA-2motif* dataset, first presented in [26], contains 1000 random Barabasi-Albert (BA) graphs where 50% of the graphs have a house motif attached to it, while the other half has a cycling motif attached to it. The aim is to classify which of the two a graph belongs to. All graphs in the dataset contain 25 nodes. Figure 8 depicts some samples.

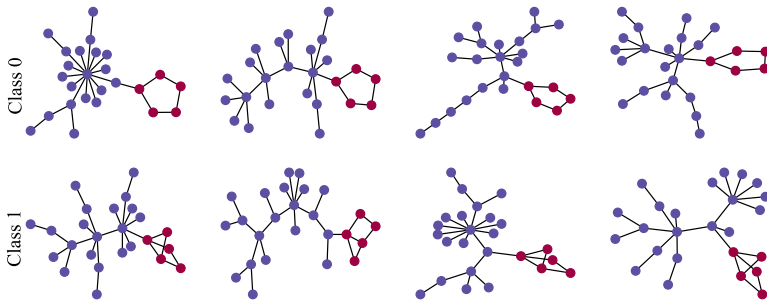
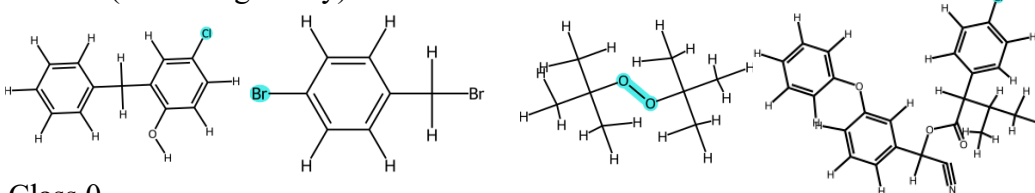


**Figure 8:** Samples from the two different classes in the BA-2motif dataset.

The *Mutag* (or *Mutagenicity*) dataset [29] consists of 1,768 molecular graphs, categorized based on their mutagenic effects on the Gram-negative bacterium *S. Salmonella*. Although the original dataset contains 4,337 graphs, we utilize a curated version from [30], which emphasizes the presence or absence of the toxicophores:  $\text{NH}_2$ ,  $\text{NO}_2$ , aliphatic halides, nitroso, and azo groups. Upon reviewing the dataset and its ground truth explanations, we observe that they are occasionally incomplete. While the labels correctly identify the relevant atoms, they often fail to account for the atomic neighborhood. For example, as illustrated in Figure 9, a chlorine (Cl) atom alone does not consistently result in

a mutagenic molecule; the mutagenicity also depends on the atomic environment around the Cl atom. However, this contextual factor is not considered in the explanation labeling of the dataset. Consequently, the absolute value of the Graph Explanation Accuracy (GEA) metric should not be overemphasized; instead, it should be interpreted in relation to other models rather than as an isolated indicator of performance.

#### Class 1 (has mutagenicity)



#### Class 0

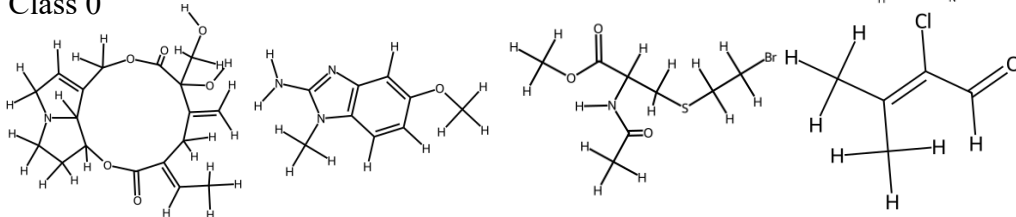


**Figure 9:** Samples from the two different classes in the Mutag dataset, with ground truth explanation labels highlighted for the positive (mutagenic) class. The figure shows that the provided explanations can be incomplete. For instance, in the top row, chlorine (Cl) or bromine (Br) atoms attached to a carbon ring are associated with mutagenicity. However, in the bottom row, molecules containing Cl or Br are non-mutagenic, indicating that these atoms alone do not always lead to mutagenicity.

## D.2 Baselines

In our experiments, we use two post-hoc explainability baselines: PGExplainer [26] and GNNExplainer [27]. Both methods aim to maximize mutual information to identify key subgraph structures influencing GNN predictions. PGExplainer employs a neural network trained on multiple data points to detect important subgraphs. In contrast, GNNExplainer learns an edge mask for each data point by optimizing the mask values through gradient descent. We use the official PyTorch Geometric [69] implementation of these models. For the hyperparameters, we follow the authors’ recommendations.

## D.3 Implementation Details

For the explainability experiments in Section 4.2, we use a three-layer GIN network [28] with a hidden dimension of 64 for the BA-2Motifs dataset. For the Mutag dataset, we use a three-layer GINE network [70], which incorporates edge features. The hidden dimension is again 64. In all experiments, the classification model and the magnetic field model share the same structure, with the only difference being that a final mean pooling layer is applied to the graph classification model.

We train the classification models using the Adam optimizer [68], with a batch size of 64 and a learning rate of  $10^{-3}$ , for a total of 500 epochs.

For our IGExplainer model, we use again the Adam optimizer [68] with a batch size of 64 and a learning rate of  $10^{-3}$  and train for 300 epochs. The model with the lowest cross-entropy loss (see Equation (20)) is saved. In these explainability experiments, we evaluate the model on the training set rather than using a separate test set. The focus of explainability is to interpret and understand the behavior of the trained model, not to assess its performance on new data.

## D.4 Extra Results

When taking samples of the IGExplainer, every sample will differ since the Ising model is stochastic. This is visualized in Figure 10 for one graph in the BA-2motif dataset. We also visualize several samples from the distribution and the sample average, i.e., approximately the marginal probability of including a node. This differs from the magnetic field  $h_\theta(\cdot)$ .

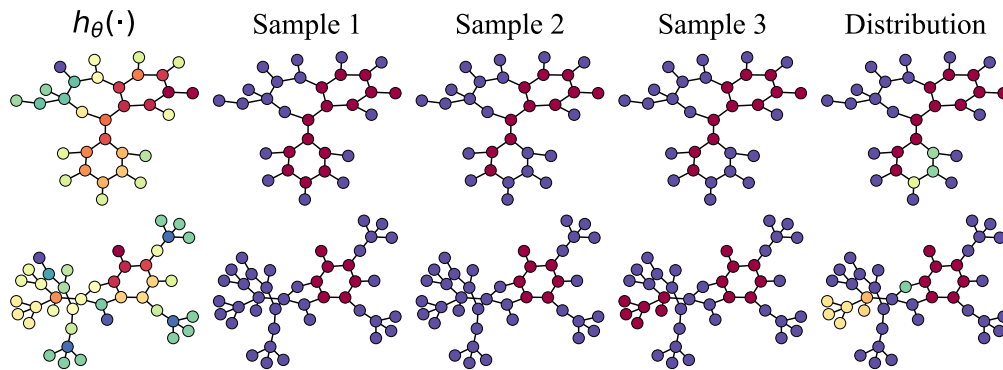


**Figure 10:** Samples from the trained IGExplainer. The distribution of the samples is different from the magnetic field  $h_\theta(\cdot)$ .

Additional predictions from the IGExplainer on the Mutag dataset are presented in Figure 11.

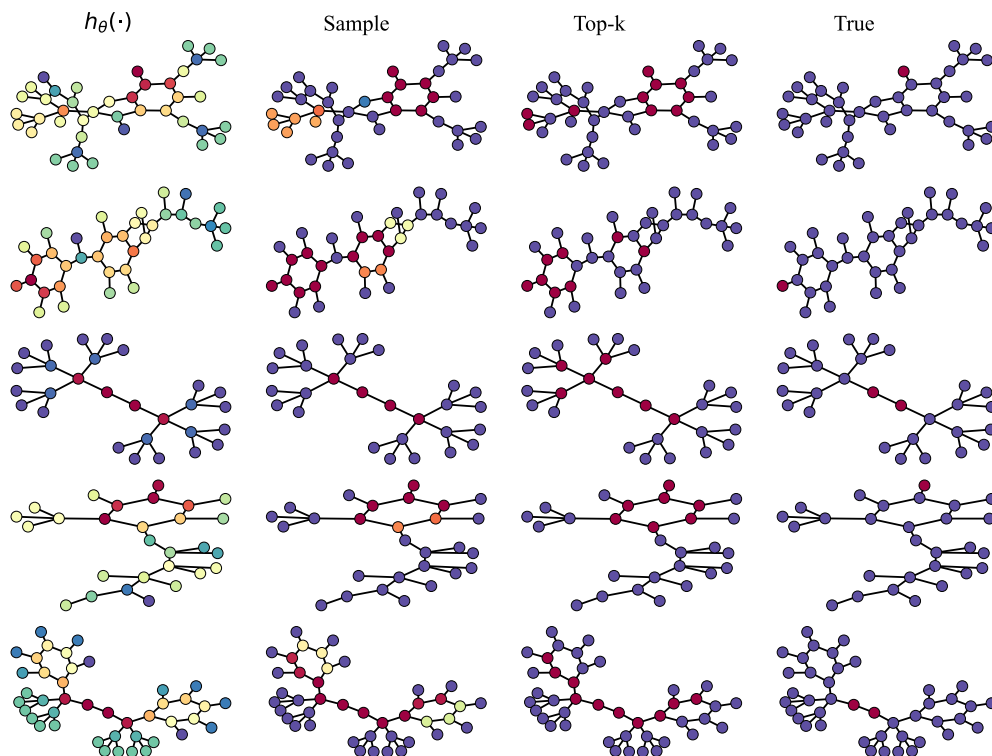


**Figure 11:** Output of the IGExplainer on the Mutag dataset. From left to right: the predicted magnetic field  $h_\theta(\cdot)$ , the sample distribution, the top-25% of nodes where  $h_\theta(\cdot)$  is the score, and finally the ground truth.



## E Mesh Coarsening

This section contains extra information on the mesh coarsening experiments of Section 4.3.

### E.1 Dataset

The details of the mesh dataset are presented in Table 3.

**Table 3:** Details of the meshes in the dataset used in Section 4.3. The table presents the mean number and the standard deviation in parentheses.

DATASET	BUST	FOURLEG	HUMAN	CHAIR
NUMBER OF VERTICES	25662 (1230)	9778 (3671)	8036 (4149)	10154 (999)
NUMBER OF FACES	51321 (2460)	19553 (7342)	16070 (8302)	20313 (2002)

### E.2 Implementation Details

The equivariant graph neural network is constructed using the *e3nn* library [35]. As the node input, we derive the mesh Laplacian according to

$$\mathbf{C}_{ij} = \begin{cases} w_{ij} = \frac{\cot \alpha_{ij} + \cot \beta_{ij}}{2}, & \text{if } i, j \text{ is an edge,} \\ -\sum_{j \in N(i)} w_{ij}, & \text{if } i \text{ is in the diagonal,} \\ 0, & \text{otherwise,} \end{cases} \quad (24)$$

where  $\alpha_{ij}$  and  $\beta_{ij}$  denote the two angles opposite of edge  $(i, j)$  [71]. We get a measure of the curvature of the node using

$$z_i^0 = \left\| \sum_{j \in N(i)} \mathbf{C}_{ij} (\hat{r}_i - \hat{r}_j) \right\|_2^2, \quad (25)$$

where  $\hat{r}_i$  is the position of node  $i$ . We use  $z_i^0$  as the model node input. As edge attributes, we use the spherical harmonics expansion of the relative distance between node  $i$  and its neighbors  $j$ ,  $Y((\hat{r}_i - \hat{r}_j) / \|\hat{r}_i - \hat{r}_j\|)$  and the node-to-node distance  $d_{ij} = \|\hat{r}_i - \hat{r}_j\|$ . We construct an equivariant convolution by first deriving the message from the neighborhood as

$$\hat{z}_i^{k+1} = \frac{1}{n_d} \sum_{j \in N(i)} z_j^k \otimes_{f_W(d_{ij})} Y\left(\frac{\hat{r}_i - \hat{r}_j}{\|\hat{r}_i - \hat{r}_j\|}\right), \quad (26)$$

where  $n_d$  is the mean number of neighboring nodes of the graph. For a triangular mesh, the degree is commonly six. The operator  $\otimes_{f_W(d_{ij})}$  defines the tensor product with distant dependent weights  $f_W(d_{ij})$ ; this is a two-layer neural network with learnable weights  $w$  that derives the weights of the tensor product. The node features are then updated according to

$$z_i^{k+1} = z_i^k + \alpha \cdot \hat{z}_i^{k+1}, \quad (27)$$

where  $\alpha$  is a learnable residual parameter dependent on  $z_i^k$ . We took inspiration for the model from the *e3nn* homepage, see [https://github.com/e3nn/e3nn/blob/main/e3nn/nn/models/v2106/points\\_convolution.py](https://github.com/e3nn/e3nn/blob/main/e3nn/nn/models/v2106/points_convolution.py).

We construct a two-layer equivariant network where the layer irreducible representations are  $[0e, 16x0e + 16x1o, 16x0e]$ . This means that the input (0e) consists of a vector of 16 scalars, and the hidden layers consist of vectors with 16 scalars (16x0e) together with 16 vectors (16x1o) of odd parity. This, in turn, maps to the output vector of 16 scalars (16x0e). We subtract the representation with the mean of all nodes in the graph and finally map this representation to a single scalar output. Here, the Ising model uses a temperature of one and  $J = -1$ .

For optimization, we employ the Adam optimizer [68] with a learning rate of 0.001 and a batch size of one. We train the model until convergence on the training set but with a maximum of 50 epochs. We did not use a validation set as there were no indications of overfitting.

### E.3 Baselines

We compare our ISING+MAG model to five other sampling methods.

- RANDOM is regular random sampling, where every node has a 50% chance of being sampled, and the samples are independent.
- FPS stands for furthest point sampling [38, 72]. FPS selects a subset of points from a point cloud by iteratively choosing the point farthest from the already selected points.
- POINT SAMPLER is the point sampler in [73], which uses a traditional GNN approach. It aimed to be faster than the iterative FPS and be better than random sampling by using a GNN with a specific *DevConv* layer to evaluate each point’s importance by analyzing its deviation from neighboring points.
- SPECTRAL is based on spectral coarsening [6], which uses the polarity of the largest Laplacian eigenvector, which, just as the Ising models, aims to find an “every other” pattern.
- ISING is the Ising model, but where the magnetic field is set to zero, resulting in a model that aims to sample in an “every other” pattern.

These methods cannot be trained for specific downstream tasks; they are inherently designed to distribute samples across the mesh evenly rather than optimize for particular applications.

### E.4 Training Time

Table 4 presents the ISING+MAG and POINT SAMPLER training times. The extended training time for ISING+MAG is primarily due to the need to coarsen the mesh to compute the loss.

**Table 4:** Training time per epoch (in seconds) for the mesh sparsification problem. We train the ISING+MAG model for 40-60 epochs and the point sampler for 150. The largest part of the time comes from redrawing the edges in the coarse mesh.

DATASET	BUST	FOURLEG	HUMAN	CHAIR
ISING+MAG	35.22	9.32	11.82	12.99
POINT SAMPLER	0.48	0.174	0.162	0.213

### E.5 Extra Results

The outcome of the experiments presented as a bar chart in Figure 4 is presented in Table 5.

**Table 5:** Mean and standard deviation of the test vertex-to-mesh distance from the five-fold cross-validation of the four datasets. Lower is better.

DATASET	BUST	FOURLEG	HUMAN	CHAIR
ISING+MAG	<b>0.221</b> (0.042)	<b>0.339</b> (0.034)	<b>0.366</b> (0.031)	<b>0.369</b> (0.046)
ISING	0.288 (0.055)	0.411 (0.034)	0.409 (0.033)	0.548 (0.045)
RANDOM	0.343 (0.064)	0.498 (0.032)	0.498 (0.032)	0.592 (0.040)
SPECTRAL	0.290 (0.056)	0.415 (0.034)	0.412 (0.034)	0.569 (0.054)
POINT SAMPLER	0.298 (0.057)	0.476 (0.034)	0.494 (0.034)	0.576 (0.046)
FPS	0.303 (0.059)	0.395 (0.029)	0.417 (0.015)	0.619 (0.059)

The results presented in Table 5 show that the Ising model with the magnetic field (ISING+MAG) surpasses all other models regarding the point-to-mesh distance. This outcome aligns with expectations, given that our model is trained for this specific task. Their results are virtually identical when comparing the Ising model without the magnetic field (ISING) to Spectral coarsening (SPECTRAL). This is anticipated since both approaches result in an every-other pattern. In SPECTRAL, nodes are chosen based on the polarity of the largest eigenvector of the graph Laplacian, which divides the nodes into two equally large subgroups.

While the furthest point sampling (FPS) method ensures that samples are distributed across the graph, it has its limitations. In some datasets, it may outperform ISING and SPECTRAL. However, it’s important to note that FPS does not guarantee an “every other” pattern and may inadvertently miss nodes in critical areas of the mesh.

Overall, the Ising model with the magnetic field (ISING+MAG) outperforms all other models. Similar to ISING and SPECTRAL, it samples an “every other” pattern. However, leveraging a geometry-aware network also learns to identify nodes crucial for maintaining mesh shape. This behavior, which defaults to using the “every other” pattern and selectively samples nodes based on the geometric shape of surrounding nodes, contributes to the model’s effectiveness.

Examples of how the Ising model learns important areas of the mesh are presented in Figures 12, 13, 14, and 15. Here, we visualize the magnetic field from the test split from the four datasets. An illustration of the course meshes after sampling is presented in Figure 16.

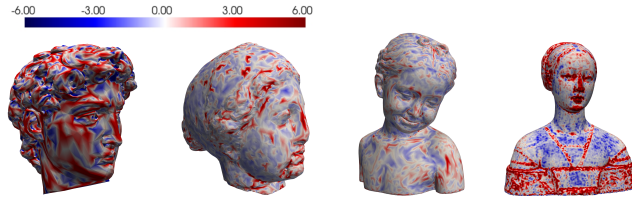


**Figure 12:** Examples of the magnetic field from the bust dataset (test set).

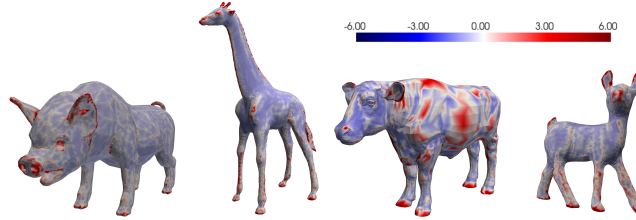


**Figure 13:** Examples of the magnetic field from the fourleg dataset (test set).

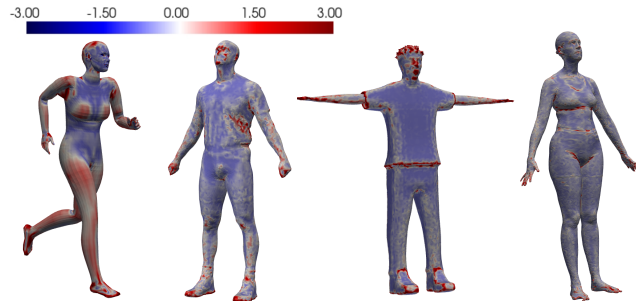


**Figure 14:** Examples of the magnetic field from the human dataset (test set).

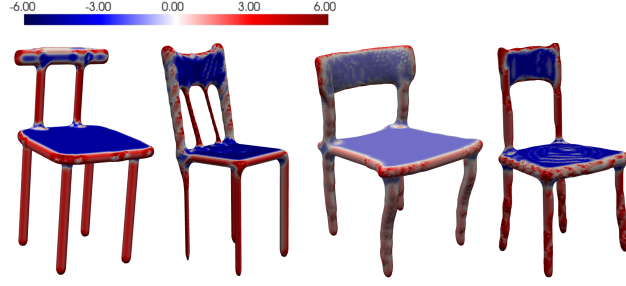


**Figure 15:** Examples of the magnetic field from the chair dataset (test set).

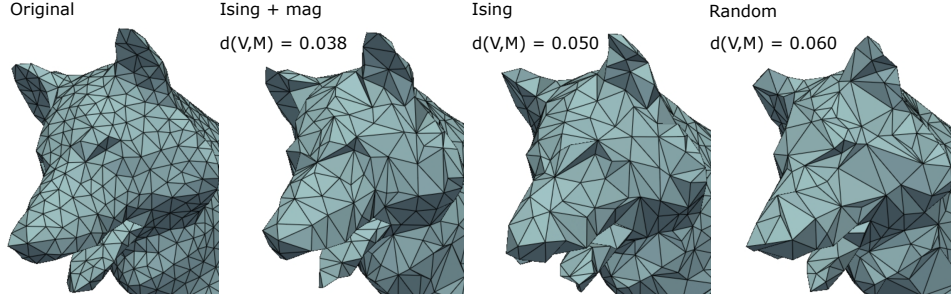


**Figure 16:** The coarsened mesh using random subsampling, Ising subsampling, and learned Ising subsampling of the nodes. The point-to-mesh distance is reduced from 0.06 to 0.038 when going from the random subsampling to the learned Ising graph. The time it takes to sample and create the course mesh is random, 1.37 sec, Ising 0.67 sec, and Ising+mag 1.31 sec. Random sampling takes longer due to a more complicated course mesh creation.

**Complexity.** Given the large graphs in mesh processing, evaluating time complexity is crucial. We measure the time complexity for coarsening and sampling to complement the results in Table 5. Figure 17 shows the sampling time alone, excluding mesh reconstruction, as a function of the mesh size. Notably, only random sampling and the neural network-based point sampler are faster than the Ising model. The relatively efficient scaling of the Ising model is due to two factors: (i) the parallelism enabled by the Metropolis-Hastings algorithm through graph coloring, and (ii) the fast convergence of the Ising model, which requires only a few iterations of the Metropolis-Hastings algorithm.

Figure 18 illustrates the combined time for sampling and coarsening. It shows that the Ising model’s coarsening time is lower than that of random sampling. This is because coarsening is less efficient with unevenly distributed samples. Additionally, coarsening is the major time factor, while the sampling time is negligible.

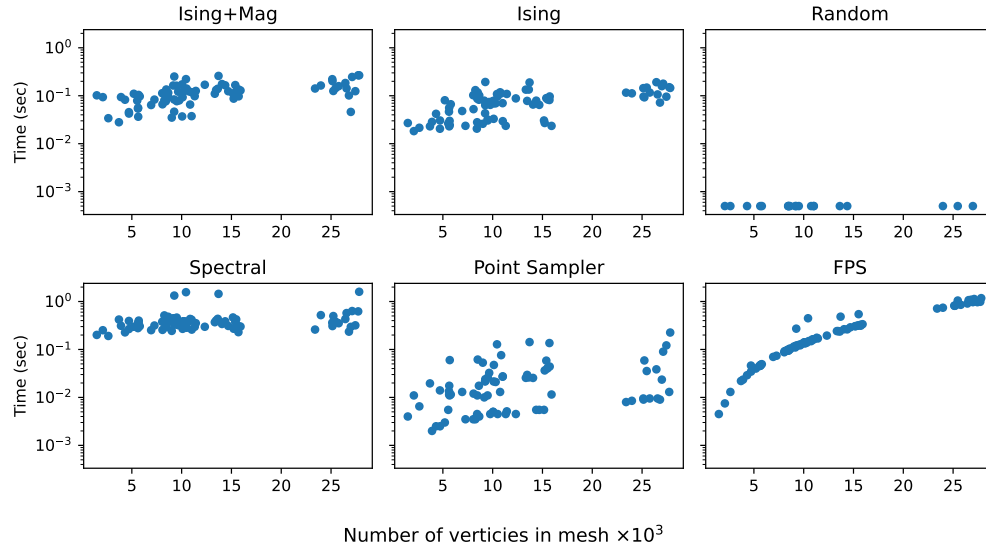


**Figure 17:** The time it takes to get sample nodes to include in the coarse graph.

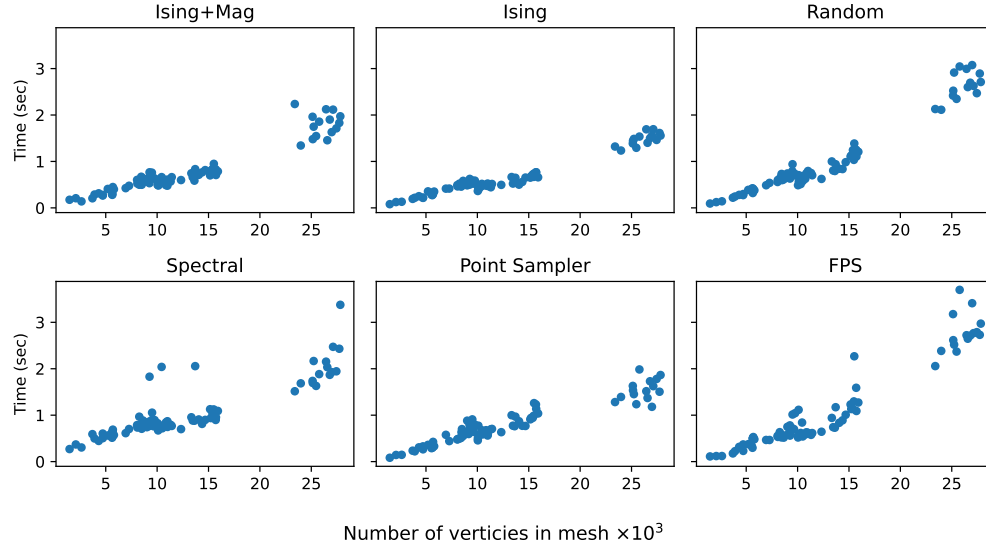


**Figure 18:** The time it takes to sample and coarsen the graph, plotted against the number of vertices in the graph.

## F Sparse Approximate Matrix Inverses

### F.1 Results and Implementation Details

With our initial model architecture, the graph representation induces an a priori assumption on the sparsity pattern of the predicted sparse approximate inverse in which we aim to select 50% of the elements in the sparsity pattern of  $A + A^2$ . Our approach is, however, not limited to the choice of an a priori sparsity pattern. Implementation-wise, we lift this constraint by adding an extra edge feature consisting of an all-ones  $n \times n$  matrix in the graph representation of the input matrix, allowing for a selection of 50% of all matrix elements in the sparse approximation of the inverse. As the a priori sparsity pattern is already incorporated into the graph representation of the input matrix, our method is flexible in choosing an a priori sparsity pattern, which should be denser than the desired sparsity level. This flexibility is especially important for computational efficiency in use cases involving large matrix dimensions.

Given the current state of the trainable parameters, two samples from the Ising model are required during training to obtain the gradient estimate. Evaluation is carried out using a single sample. In both cases, the sample  $x$  from the Ising model produced after  $T$  MCMC iterations is passed to the final layer, which solves the  $n$  optimization problems,

$$s_k^* = \arg \min_{s_k' \in \mathcal{R}^{m_k}} \|AM_k(s_k) - I_k\|_2^2, \quad (28)$$

computing the values  $s_k^* \in \mathbb{R}^m$  of the non-zero entries of each column  $M_k$  of  $M$ . Thus, the final output is the predicted sparse approximate inverse  $M$ . Empirically,  $T = 3$  is found to be sufficient.

Independent on which dataset is used, 60% of the samples are used for training, and the remaining 40% are divided equally between a validation set and a test set. We use the magnetic field-dependent regularization described in Section 3 to optimize for a sampling fraction of 50% of the a priori sparsity pattern. The sampling fraction converges to an average value close to 50% in all settings with the proposed regularization scheme. The mean recorded sampling fraction on the test dataset in *Setting 1* and *Setting 2* is 52.4% and 50.9%, respectively. The corresponding sampling fraction in *Setting 3* is 49.8%. The baseline methods are tuned to allow for the same sampling fraction during evaluation.

Results for two samples from the test dataset in *Setting 3* are visualized in Figure 5. The first sample (top) shows the predicted sparsity pattern when the true inverse is dense. For this sample, the recorded loss is 2.61 (ISING+MAG) compared to 3.57 (Ising), 4.18 (Random) and 4.12 (Only A). As discussed in Figure 1, the magnitude of the local magnetic field influences the sampling probability in that region, which can be seen by comparing the output magnetic field to the obtained sparsity pattern for both samples. A zero magnetic field in the Ising model can be interpreted as a prior on the sparsity pattern in which 50% of the elements in each row and column of the matrix are selected, resulting in an inverse approximation in which the nonzero elements are evenly distributed across the given matrix. For the second sample (bottom), the sparsity optimized for is lower than the sparsity of the true inverse. We choose to display this sample as the results clearly illustrate that the learned magnetic field indeed results in an Ising model from which the sampled sparsity pattern successfully avoids the most unimportant regions in the true inverse for the particular input matrix. For this sample, the recorded loss is 1.02 (ISING+MAG) compared to 3.75 (Ising), 3.76 (Random) and 4.06 (Only A).

### F.2 Graph Convolutional Neural Network

Here, we use the simple and deep graph convolutional networks from Chen et al. [43] where we set the strength of the initial residual connection  $\alpha$  to 0.1 and  $\theta$ , the hyperparameter to compute the strength of the identity to 0.5. The network contains four layers, each with a hidden dimension of 64. We utilize weight sharing across these layers. The dimension of the output of the final convolutional layer is 64. This output is subtracted with the mean of the node values before a final linear layer reduces the size to one.

We employ the Adam optimizer [68] with a learning rate of 0.01 for optimization. We train the model until convergence on the training set but with a maximum number of 300 epochs, as there were no indications of overfitting. Here, the Ising model uses a temperature of one and  $J = -0.4$ .

The training times per epoch were 1 minute for *Setting 1* and three minutes for *Setting 2* and *Setting 3*, respectively. These models converged in less than 50 epochs.

### F.3 Datasets

**Dataset 1.** This is a synthetic dataset containing 1600 binary matrices. Each matrix is real, symmetric, and of dimensionality  $30 \times 30$ . The matrices in the dataset are automatically generated based on the principle that the probability of a nonzero element increases towards the diagonal, with 100% probability of nonzero diagonal elements. The upper right and lower left corners have a very low probability of being nonzero, and in between these elements and the diagonal, the probability of a nonzero element varies according to a nonlinear function. The mean sparsity is 83% zero-elements in the generated dataset. The maximum sparsity allowed in the data-generating process is 96%, and the determinant of each matrix is bounded between 0.001 and 50. Figure 19 shows sparsity patterns of four matrices in the final dataset.

The dataset is available upon request and will be released together with the code used for preprocessing and generation.

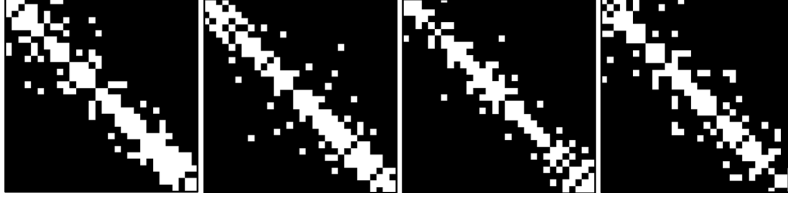


**Figure 19:** Example of samples from *Dataset 1*. Nonzero elements are represented in white.

**Dataset 2.** This synthetic dataset contains 1800 submatrices of size  $30 \times 30$  constructed from the SuiteSparse Matrix Collection [44]. Since the original matrices in the dataset are often denser closer to the diagonal, the submatrices are constructed by iterating a window of size  $30 \times 30$  along the diagonals, such that no submatrix overlaps another submatrix. To ensure that each submatrix is symmetric, only the upper triangular part of the matrix is used to create each matrix. Each submatrix is scaled such that the absolute value of the maximum element is one, and submatrices with all values below  $10^{-6}$  are removed from the dataset. The mean sparsity in the final dataset is 89%. The maximum sparsity allowed in the data-generating process is 96%, and the determinant of each matrix is bounded between 0.001 and 50. Figure 20 shows sparsity patterns of four matrices in the final dataset.

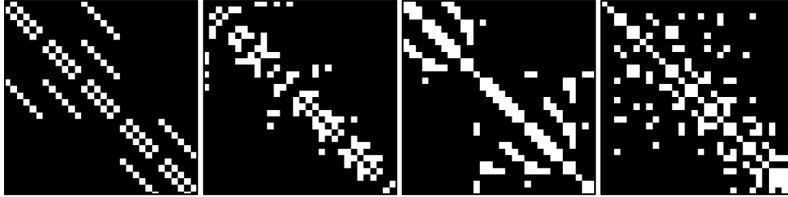


**Figure 20:** Example of sparsity patterns of samples from *Dataset 2*. Nonzero elements are represented in white.

The original dataset is under the CC-BY 4.0 License. Our modified dataset is available upon request and will be released with the code used for preprocessing and generation.